Sub-wavelength effects in a free electron laser oscillator

P. Pongchalee[1,2,3,*] AND B. W. J. McNeil[1,2]

[1]*Department of Physics, University of Strathclyde (SUPA), Glasgow G4 0NG, UK*
[2]*Cockcroft Institute, Warrington, WA4 4AD, UK*
[3]*ASTeC, STFC Daresbury Laboratory, Warrington, WA4 4AD, UK*
[*]*pornthep.pongchalee@strath.ac.uk*

Abstract: Previous simulation studies of cavity based free electron lasers (FELs) have utilised models which average the optical field in the FEL interaction over an integer number of radiation wavelengths. In this paper, two unaveraged simulation codes, OPC and Puffin, are combined to enable modelling, for the first time, of a cavity based FEL at the sub-wavelength scale. This enables modelling of effects such as coherent spontaneous emission from the electron beam and sub-wavelength cavity length detuning. A cavity FEL operating in the mid-infrared is modelled and it is shown that, for small sub-wavelength cavity detunings, the FEL can preferentially lase at the third harmonic of the fundamental FEL wavelength. This novel result suggests other modes of operation may be possible and opens up cavity-based FEL operation to investigation of further, potentially useful, modes of operation.

1. Introduction

Free electron lasers (FELs) are a powerful, tunable and versatile radiation source from the microwave through to the hard X-ray regions of the spectrum and, as such, have a wide-range of current and potential applications in science and industry. FELs can operate either as a high-gain, single pass, amplifier or in a lower-gain oscillator mode which requires the FEL undulator to be placed within a cavity to provide radiation feedback.

The work presented here considers the FEL oscillator regime of operation. The performance of such FELs is influenced by a variety of factors, including the design of the cavity resonator, the properties of the electron beam and the undulator. The cavity resonator length is the distance between its mirrors and is a critical parameter that requires adjustment to ensure that the radiation emitted by a previous electron pulse overlaps with the next electron pulse as it enters the FEL undulator. When the round-trip time of a radiation pulse within the cavity is equal to the difference in arrival times between electron pulses, the cavity is said to be resonant. The cavity length can be 'detuned' away from this resonant length to alter and improve radiation output for specific applications.

One notable advantage of cavity detuning is its ability to be implemented in existing FEL facilities without the need for significant structural changes. Additionally, the cavity length can be dynamically adjusted in real-time while the FEL is operating, providing additional control over output parameters, such as intensity and efficiency, enabling its performance to be optimised for specific applications [1].

In this paper, unaveraged simulations are used to investigate, for the first time, the effects of cavity detuning at the sub-wavelength scale in an FEL oscillator. This requires a sub-wavelength resolution of the radiation/electron FEL interaction which is not available via averaged computational models that average the FEL interaction over an integer number of radiation wavelengths. When simulating short pulses, both the coherent and shot-noise spontaneous

emission of the electron beam [2] are included in the simulation. Coherent spontaneous emission (CSE) has the potential to dominate the FEL start-up amplification in an undulator, especially in the low-gain regime of FEL operation [3]. CSE is primarily induced by a short electron pulse with a fine current structure at the wavelength scale, such as a rectangular beam current with 'sharp edges'. Therefore, a more thorough understanding of these sub-wavelength effects is required, particularly for short-pulse FEL oscillators, and a preliminary investigation is presented here in the mid-IR region of the spectrum.

The unaveraged FEL simulation code Puffin [4,5] (available from [6]), and the optical propagation code (OPC) [7,8] (available from [9]), were previously combined to simulate a regenerative amplifier FEL (RAFEL) oscillator [10] in the steady-state region of operation, where periodic boundary conditions were applied to the electron-radiation interaction so that all pulse effects, such as CSE, were absent. By using the combined Puffin-OPC modelling in a pulsed mode of operation, wide-bandwidth and sub-wavelength effects, such as harmonic radiation generation, CSE and sub-wavelength cavity detuning, can be modelled. This results in a complete, 3D un-averaged computational model of a short-pulse FEL oscillator, and its initial results are presented here for the first time.

Some of the effects of sub-wavelength cavity detuning on FEL performance are examined, and in particular its effects upon harmonic generation within the FEL oscillator. Generation of radiation at the third harmonic of the fundamental resonant wavelength in an FEL was first demonstrated by introducing a dispersive material into the cavity of an FEL oscillator to alter the round-trip transit times between the fundamental and third harmonic pulses within the cavity [11].

The simulation results presented here, using both a 'sharp' rectangular electron beam current profile and a 'smooth' Gaussian profile electron beam, consistently show that cavity detuning at a sub-radiation wavelength scale can increase harmonic radiation output above that of the fundamental mode to achieve harmonic lasing without the need for any dispersive materials. These findings suggest that harmonic lasing emerges as a result of sub-wavelength cavity detuning and not exclusively from the CSE from a sharp edged beam current. An FEL oscillator operating in the mid-infrared is simulated to demonstrate this novel mode of FEL operation.

2. Simulation model

2.1. FEL and optics code

The work of [10] gives an overview of the unaveraged simulation method for FEL oscillators. The method uses two simulation codes, Puffin and OPC, which simulate the electron/radiation interaction in the FEL undulator and the propagation of the resulting radiation field through the oscillator cavity, respectively. Puffin is an unaveraged FEL simulation code, which simulates the interaction between electrons and light in an undulator. Following the Puffin FEL simulation the output field at the undulator exit is then translated into OPC code format which then simulates the propagation of the radiation field through the optical oscillator cavity, including mirrors and other optical elements. The two codes are run sequentially, starting with the Puffin simulation of the FEL interaction. The OPC simulation of the radiation through the oscillator cavity then allows adjustment of the optical path length due to cavity detuning. Following OPC propagation to the undulator entrance, the radiation field is translated back into a format which serves as the seed field for the input into the next pass through Puffin. This iterative process, pass by pass, allows an accurate simulation of the FEL interaction and propagation of the radiation field through the optical elements of the oscillator cavity.

2.2. Simulation parameters

In the example presented here, the parameters used are given in Table 1 and are very similar to those of the one-dimensional simulations of the IR-FEL presented in [12], but with the additional optics and beam parameters required to model in three-dimensions. A curved-pole undulator focussing is used to maintain a constant transverse electron beam size throughout the undulator length [13,14]. The undulator module of length 1.8 m has 40 periods of wavelength $\lambda_u = 4.5$ cm. The matched transverse electron beam size in the undulator focusing is then $\sigma_{x,y} = (\epsilon_{x,y}\lambda_u/(\sqrt{2}\pi a_w))^{1/2}$, where $\epsilon_{x,y}$ is the normalised emittance of the beam, λ_u is the undulator period, and a_w is the RMS undulator parameter, so that $\sigma_{x,y} = 311.8$ μm. The temporal shape of the current of each electron pulse in the beam is rectangular of duration 400 fs. The mean electron beam energy is γ in units of $m_e c^2$, to give a resonant radiation wavelength, $\lambda_r = \lambda_u(1 + a_w^2)/2\gamma^2 \approx 6$ μm, in the mid-infrared. Each electron pulse in the beam then has a length of $20\lambda_r$. For the resonant cavity condition, the time between two consecutive electron pulses must be matched to roundtrip time of the cavity, so that $c/f_{rep} = 2L_{cav}$, where f_{rep} is a electron pulse repetition rate, and L_{cav} is the cavity length between two mirrors.

The 2-mirror optical cavity is designed as a near-concentric resonator with a Rayleigh range of 52 cm, as shown in Fig. 1. The first mirror M_1 is placed after the undulator exit with an output coupling that can be partially transmissive or use a hole out-coupling. The second mirror M_2 that forms the simple cavity is then placed before the undulator entrance. When the distance between the two mirrors gives a round-trip propagation time equal to the electron beam repetition rate, the cavity has zero length detuning. The optical beam waist position is placed at the centre of the undulator and the Rayleigh range is approximately one-third of the undulator length.
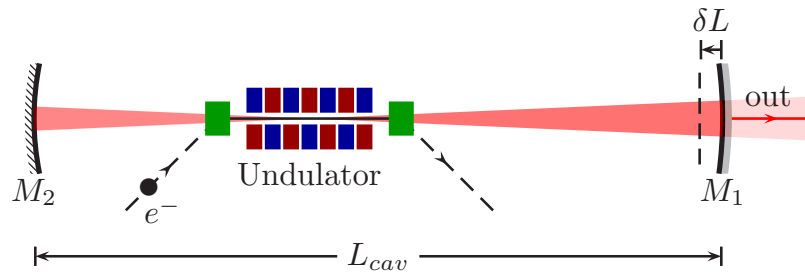

Fig. 1. Schematic of the FEL oscillator as used in the simulation. The cavity, formed by the two mirrors M_1 and M_2, can be changed in length by the cavity detuning parameter δL. This adjusts the synchronisation between the electron pulse arrival times and the radiation round-trip time in the cavity which are synchronous when $\delta L = 0$.

Radiation propagation in the optical cavity is modelled using the OPC simulation code [7,8]. The choice of the code's radiation propagation method, among other factors, plays a fundamental role in the accuracy of the simulation. Three propagation methods, namely the spectral method, Fresnel diffraction integrals, and modified Fresnel integrals, can be implemented in OPC. Of the three methods, the spectral method and Fresnel diffraction integrals can be solved numerically using fast Fourier transforms (FFTs). In contrast, the modified Fresnel integral, while yielding valuable results, is the least efficient method [7]. However, it does provides a promising alternative as it facilitates the propagation of an optical beam through a complex optical system in a single step. A prerequisite for the successful application of this method is that all optical components must be accurately described by an ABCD matrix [15]. Additionally, the scaling applied to this method enables the use of a magnification factor for the grid, which allows for the application of different transverse mesh sizes at the Puffin input and cavity mirror output planes.

Table 1. Summary of FEL oscillator parameters used in the simulations

Electron beam parameters		Rectangular	Gaussian
Electron energy (MeV)	50		
Bunch charge (pC)	100		
Normalised emittance, $\sigma_{x,y}$ (mm mrad)	12/12		
Energy spread	0.5%		
Bunch length (fs)		400	470 (FWHM)
Peak current (A)		250	200
Transverse size, $\sigma_{x,y}$ (μm)	311.8		
Bunch repetition (MHz)	10		
Undulator			
Undulator type	Curved pole		
Polarisation	Linear		
Undulator parameter (rms)	1.25		
Pitch (cm)	4.5		
Number of periods	40		
Oscillator			
Rayleigh range (m)	0.52		
Cavity length (m)	14.9896		
Mirror 1 radius (m)	9.00024		
Mirror 1 reflectivity	0.960		
Mirror 2 radius (m)	6.064		
Mirror 2 reflectivity	0.999		
Waist position (m)	6.02		
FEL			
FEL parameter (ρ)	0.0052		

In this study, the oscillator waist position is at the centre of the undulator, so that the FEL output propagates a distance of $\sim$ 7.1 m from the undulator exit to the first mirror M_1 for a resonant cavity length. The diffraction induces significant changes in the transverse optical beam size, from $\sim$ 1 cm^2 to $\sim$ 100 cm^2 which is modelled using the OPC modified Fresnel integral algorithm to increase the transverse dimensions of the optical nodes by a factor of 10. To complete the round-trip of the OPC oscillator simulation, the reflected optical beam from M_1 is then propagated to M_2, and then back to the undulator entrance where the transverse node size is then reduced by a factor of 10 and converted into the Puffin input format, before the next pass through the Puffin FEL simulation.

3. Simulation results

The simulation methods and parameters of Section 2 are now used to model the FEL oscillator. Figure 2 shows the position of the rectangular current electron pulse at the beginning of the undulator as well as the evolution of the radiation power, and phase during the first pass through the cavity. The trailing edge of the electron pulse generates a CSE wavefront at a temporal position of $(ct - z)/\lambda_r = 20$ as it propagates through the undulator at a velocity less than c. The CSE generated by the rectangular current profile electron pulse propagates vertically at the temporal position of 20 wavelengths in the figure and has a greater power than the spontaneous power due to shot-noise.
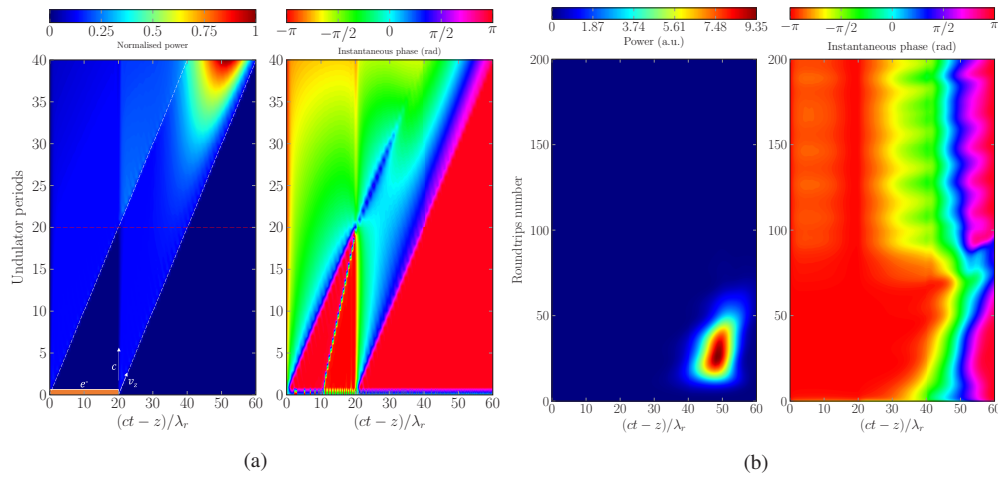
Fig. 2. (a) Contour plot of the normalised FEL power evolution (left) and phase (right) as the electron pulse propagates through the undulator during the first pass through the oscillator. The plot is in a window travelling at the speed of light, so that the electron beam of length $20\lambda_r$ (initially bottom left) moves left-to-right in the radiation window frame as it propagates through the undulator, as shown by the white dashed lines. The radiation power starts from both electron beam shot-noise and coherent spontaneous emission. (b) Contour plot of the scaled FEL power $\bar{P}$ evolution as a function of the number of round-trips within the oscillator cavity for zero cavity detuning, $\delta L = 0$. It is seen that the radiation pulse power drifts from left to right in the window between increasing round-trip number 10 - 50, indicating that its net velocity is less than the speed of light. This causes a slow decoupling with the electron pulse after each round trip and the radiation power is seen to decrease after round trip ~ 25.

Towards the end of the undulator, the radiation gain is seen to occur towards the rear of the window where the electrons are more bunched due to the FEL interaction and emit more strongly. As a result, the optical pulse's centroid (at $(ct - z)/\lambda_r \approx 50$ and the phase is ≈ 0) propagates slower than the speed of light. The optical pulse centroid is then gradually retarded with each subsequent pass of an electron pulse through a resonant cavity, where $\delta L = 0$, and the optical pulse and electron beam gradually decouple over subsequent passes in the cavity.

This can be seen in the evolution of the FEL scaled power and phase as a function of cavity round-trip number shown in Fig. 2(b), where it is seen that the peak power propagates at a velocity less than c, commonly called 'gain lethargy'. From the first pass through the cavity, the pulse is amplified, reaching its peak energy at pass number ~ 20, then gradually decays until decoupled from the electrons at pass number ~ 80. This radiation pulse evolution behaviour for the zero cavity detuning case $\delta L = 0$ is in agreement with the analytic model of short pulse evolution in a FEL oscillator [16].

Cavity detuning can be used to adjust the timing between the optical pulse and the electron bunch in an undulator, compensating for the delay caused by the gain lethargy in FEL oscillators [16,17]. By shortening the cavity, the optical pulse arrives earlier in time to the electron bunch, reducing the gain lethargy and improving FEL interaction performance. Additionally, this shortening of the cavity can also give more control of the temporal characteristics of the FEL pulse.

In this study, a positive cavity detuning of $\delta L > 0$ is used to represent a shortening of the cavity, as shown in Fig. 1. This means that the light pulse travels a reduced distance of $2\delta L$ for each round-trip. Puffin, the unaveraged FEL code, allows for a sub-wavelength adjustment of

cavity detuning with a minimum resolution equal to the distance between adjacent nodes of the radiation field sampling. Here, 21 nodes are used to sample each radiation wavelength within Puffin, allowing the cavity detuning δL to be changed in units of $0.05\lambda_r$, giving a cavity roundtrip distance change of the radiation of $2\delta L = 0.1\lambda_r$. The cavity detuning can then be adjusted in small, sub-wavelength increments, allowing the study of how fine-tuning of the cavity detuning at the sub-wavelength scale affects FEL output.

The oscillator model here uses Puffin scaled units [4,5] in which ρ is the fundamental FEL parameter. The scaled pulse energy is then expressed as $\bar{\varepsilon} = \int \bar{P} d\bar{z}_2$, where $\bar{P}$ is the scaled power from Puffin (see Fig. 2), $\bar{z}_2$ is the temporal scaling parameter given by $\bar{z}_2 = (ct - z)/l_c$, and $l_c = \lambda_r/(4\pi\rho)$ is the cooperation length. Note that the radiation power is related to the scaled power from Puffin via $P = s_p\bar{P}$, where $s_p = l_g l_c c \epsilon_0 ((\gamma m_e c^2)/(e\kappa l_g))^2$, $\kappa = a_w/(2\rho\gamma)$ and $l_g = \lambda_w/(4\pi\rho)$ is the gain length. The pulse energy is then $\varepsilon = s_p(l_c/c)\bar{\varepsilon}$. For example in Fig. 3, a scaled pulse energy of $\bar{\varepsilon} = 10$ corresponds to a real pulse energy of $\varepsilon \sim 0.9$ mJ.

The scaled pulse energy $\bar{\varepsilon}$ is plotted in Fig. 3 as a function of the number of cavity round-trips, for a range of cavity sub-wavelength detunings from resonance, $\delta L = 0$, and for an output mirror reflectivity of $R = 0.96$. The sub-wavelength cavity detuning range of $0 \leq 2\delta L < 0.5$ is plotted in Fig. 3(a)), where it can be seen that, for the smaller cavity detunings $2\delta L = 0.0 - 0.3\lambda_r$, the scaled pulse energy $\bar{\varepsilon}$ initially grows but then falls off for roundtrips $0 - 100$, due to the lethargy effect. For $2\delta L = 0.2$ and $0.3\lambda_r$, the pulse energy then rises again after passing roundtrip number ~ 200 before reaching a steady-state behaviour for roundtrip numbers >400. Notice the steady-state type behaviour occurs for fewer round trips (<100) with increasing cavity detuning, as seen in Fig. 3(b)). For $2\delta L > 1.0\lambda_r$, the steady-state is reached in a relatively few round-trips of <50 and is due to the FEL gain initially occurring towards the front of the electron pulse more rapidly than for smaller detunings. After reaching saturation, the pulse energy also demonstrates a limit-cycle behaviour [18], with an oscillation frequency dependant upon on the cavity detuning, as previously observed in the work of [19].
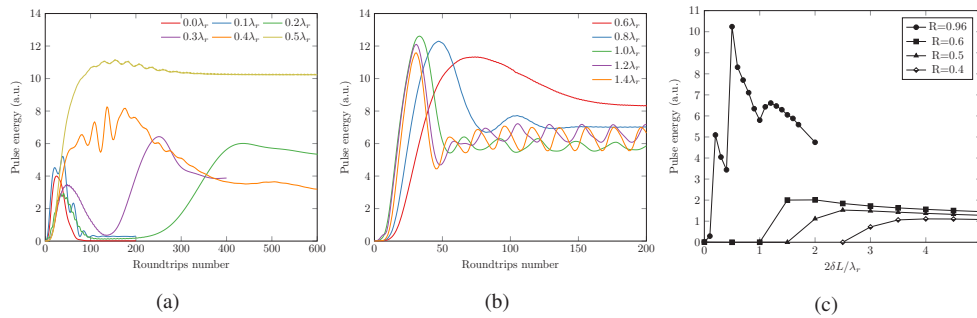

(a)　　　　　　　　　(b)　　　　　　　　　(c)

Fig. 3. Radiation scaled pulse energy $\bar{\varepsilon}$ as the function of roundtrip number for a range of sub-wavelength cavity detunings: (a) $0.0 < 2\delta L < 0.5\lambda_r$ and (b) $0.6 < 2\delta L < 1.4\lambda_r$ for the case of cavity mirror M_1 reflectivity of $R = 0.96$. Note different horizontal scales. (c) Steady-state (saturated) scaled pulse energy $\bar{\varepsilon}$ at the undulator exit from Puffin-OPC simulation Vs cavity detuning $2\delta L$ in units of radiation wavelengths for a total reflectivity $R = 0.96$. The additional plots are for cavity reflectivities of $R = 0.6, 0.5$, and 0.4.

The steady-state, post saturation pulse energies as a function of cavity detuning shown in Fig. 3(a & b), are summarised in Fig. 3(c). Also plotted are the cases for output mirror M_1 reflectivities of $R = 0.6, 0.5$ and 0.4 where the optimal cavity detunings are at $2\delta L \approx 2\lambda_r, 2.5\lambda_r$, and $4\lambda_r$, respectively, so that for decreasing mirror reflectivity, the optimum detuning for steady-state pulse energy is shifted towards larger values, in agreement with the analytical model of [20]. While only the intra-cavity behaviour is presented here, via the scaled FEL power from the

undulator exit, all of the subsequent optical cavity effects, such as diffraction and out-coupling losses, can be modelled.

The gain at the steady-state is defined by $G = (P_G - P_0)/P_0$, where P_0 is the peak radiation power measured at the undulator entrance and P_G is the peak intracavity radiation power at the undulator exit. It is assumed that a partially transmissive mirror with reflectivity R is used as the out-coupling so that the out-coupling power is then $P_{out} = (1 - R)P_G$. In this simulation, P_G is obtained from Puffin output file, while P_0 is obtained following cavity propagation using OPC. P_0 therefore includes all of the cavity effects during the propagation from the undulator exit toward the cavity mirrors and back to the undulator entrance, and can be written as $P_0 = (1 - \alpha)P_G$, where α describes the total cavity losses. In the steady-state, the gain will balance these total losses. The extraction efficiency $\eta = P_{out}/P_e$, where $P_e = \gamma mc^2 I_b/e$ is the peak electron beam power ~ 12.5 GW.

In Fig. 4 the steady-state peak power gain G_p and mean energy gain G_ε (4(a)), the FWHM pulse duration in units of λ_r, the FEL beam waist at the undulator exit in units of mm (Fig. 4(b)) and the peak (η_p) and mean energy (η_ε) extraction efficiencies (Fig. 4(c)) are plotted. For the case of a cavity detuning $2\delta L/\lambda_r = 0.2$, where lasing occurs at the third harmonic, it is seen that the steady state loss balances gain $\sim 10\%$. This is higher than the total mirror reflectivity loss of $\sim 4\%$ and is due to diffractive losses at the cavity mirrors. Where the cavity detuning $2\delta L/\lambda_r > 0.5$ it is seen that lasing occurs at the fundamental. Diffractive losses are then greater due to the longer fundamental wavelength giving an increased beam radius at the end of the undulator as seen from Fig. 4(b). However, the gain is also greater for the fundamental and compensates the diffractive losses, as seen in Fig. 4(a).
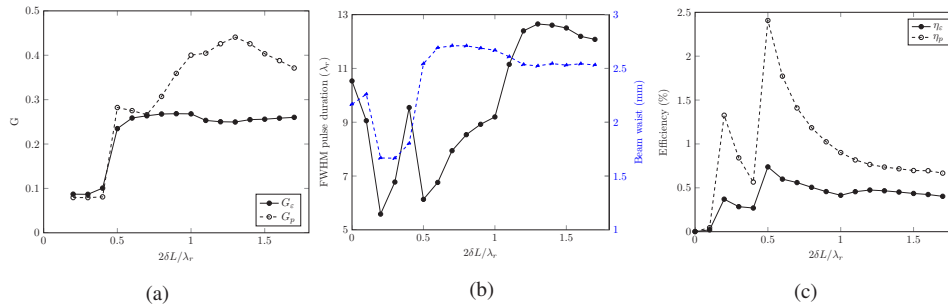

(a)   (b)   (c)

Fig. 4. The plot illutrates the results from Puffin-OPC simulations in relation to cavity detuning $2\delta L$ for a total reflectivity of $R = 0.96$. The calculated values shown include (a) peak and mean gains G_p, G_ε, (b) full-width at half maximum (FWHM) FEL pulse duration (solid line), FEL beam waist at the undulator exit (dashed blue line), and (c) extraction efficiency. In (a & c), the peak pulse powers are represented by the dashed line, while those for the mean pulse energy are represented by the solid line. Note that for the gains of a), cavity detunings $2\delta L = 0$ and 0.1 are not plotted due to the very limited lasing, as seen from the efficiencies plotted in c), leading to a noisey value.

In Fig. 3(c) it is seen that there is a departure in the saturation energies as a function of cavity detuning from previous works, e.g. that of [19], for the $R = 0.96$ case and for small, sub-wavelength cavity detunings $2\delta L/\lambda_r < 1$. In particular, there are two maxima of the saturated pulse energy around $2\delta L/\lambda_r = 0.2$ and 0.5. In order to better understand this behaviour, it is helpful to look at how the radiation field and spectral components of the FEL output pulse power for the $2\delta L = 0.2$ case evolves with cavity pass number, as shown in Fig. 5, where it can be seen that, while growth of the fundamental frequency $\omega/\omega_r = 1$ initially dominates, the third harmonic growth evolves to dominate into the steady state for larger pass numbers.
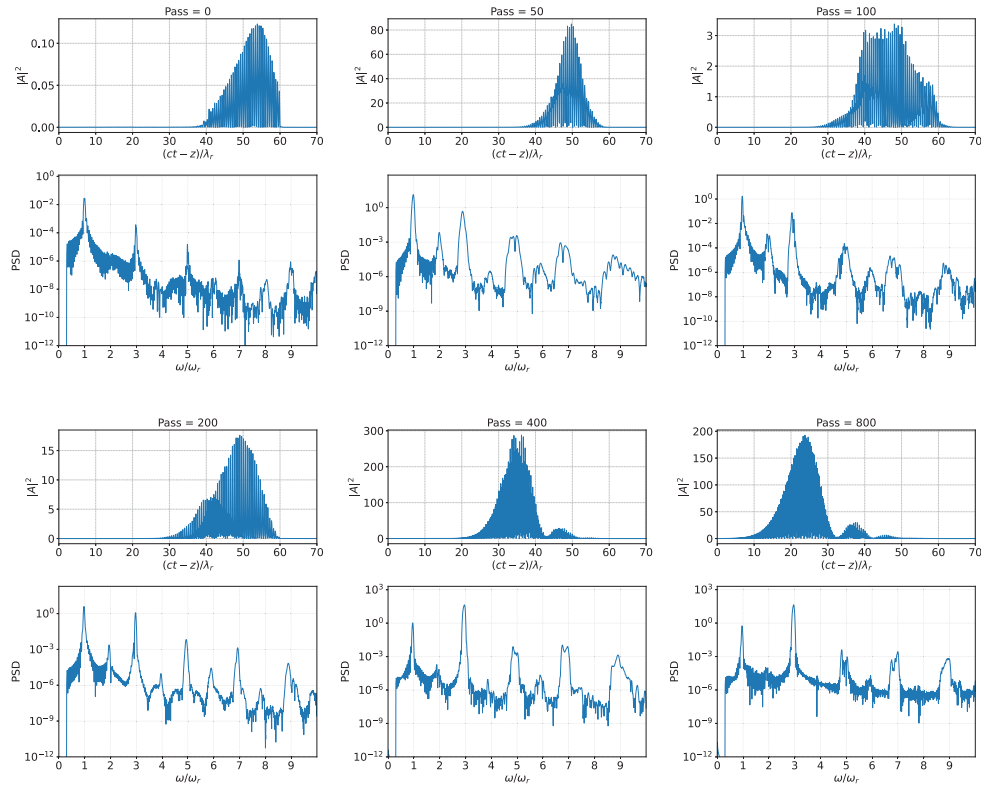
Fig. 5. The temporal, scaled power profiles, $|A|^2$, at the undulator exit for the central transverse node of the Puffin output field, and its corresponding power spectral density (PSD), for different pass numbers through the cavity for a cavity detuning of $2\delta L = 0.2\lambda_r$. It can be seen that, while there is initial growth of the fundamental $\omega/\omega_r \approx 1$, the third harmonic $\omega/\omega_r \approx 3$ evolves to dominate at larger pass numbers into the steady state.

The effect of this behaviour can be seen more clearly in Fig. 6, which plots the scaled spectral pulse energies for three cavity detunings. For the $2\delta L = 0.2\lambda_r$ case of Fig. 5, it can be seen that the pulse energy at the fundamental (solid line) has a greater initial gain and reaches a maximum amplitude after ∼ 40 roundtrips. Its gain then gradually declines due to the gain lethargy at the fundamental with an insufficient cavity detuning to compensate. However, this cavity detuning does allow the pulse energy at the third harmonic (dashed line) to be amplified over many round-trips, as can be seen in the contour plots of the instantaneous pulse power and phase for an increasing number of cavity roundtrips. The pulse phase contour evolution shows that the third harmonic pulse amplification begins to dominate after pass number ∼ 100, while the fundamental is declining due to lethargy. The third harmonic pulse then continues to be amplified from pass number ∼ 100 until it reaches a steady-state saturation for pass numbers >700. Fig. 6 also plots the evolution of the fundamental and third harmonic for cavity detunings of $2\delta L = 0.3\lambda_r$, and $0.4\lambda_r$, where it can be seen that the fundamental pulse energy evolution increases for larger cavity detunings. Increasing the cavity detuning further to $2\delta L = 0.6\lambda_r$, $0.9\lambda_r$, and $1.2\lambda_r$, as shown in Fig. 7, it is seen that the fundamental begins to dominate evolution, in agreement with [19].

In addition to simulations carried out with a rectangular electron beam current profile, which generates significant CSE powers greater than spontaneous emission due to shot-noise, simulations
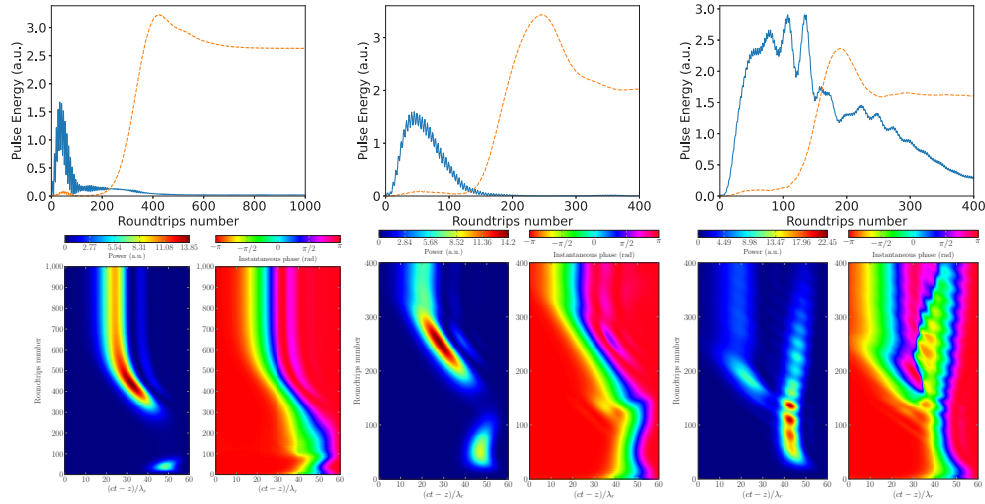
Fig. 6. (top) The fundamental (solid blue) and third harmonic (dashed red) spectral pulse energy evolution as the function of cavity roundtrip number for cavity detunings of (left to right) $2\delta L = 0.2\lambda_r$, $2\delta L = 0.3\lambda_r$, and $2\delta L = 0.4\lambda_r$. (bottom) Contour plot of the FEL pulse power and phase evolution over multiple passes for the corresponding cavity detunings.
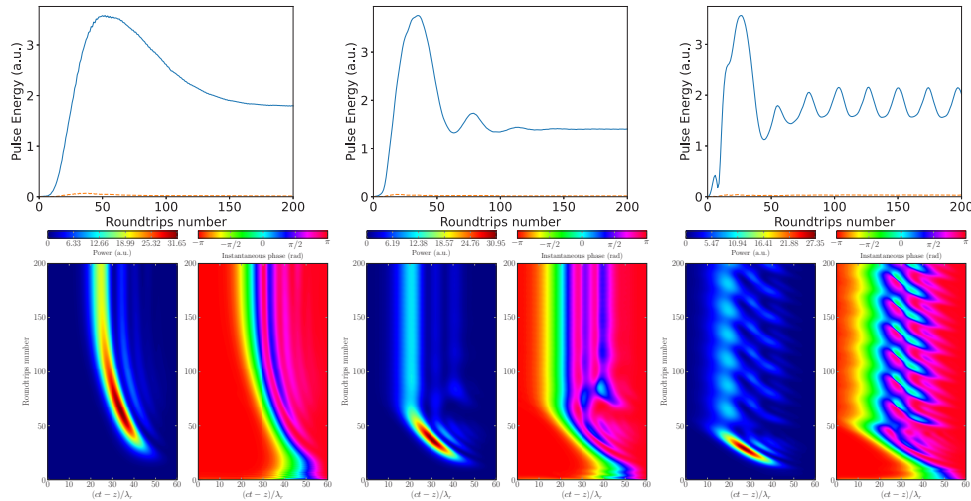

Fig. 7. (top) The fundamental (solid blue) and third harmonic (dashed red) spectral pulse energy evolution as the function of cavity roundtrip number for cavity detunings of (left to right) $2\delta L = 0.6\lambda_r$, $2\delta L = 0.9\lambda_r$, and $2\delta L = 1.2\lambda_r$. (bottom) Contour plot of the FEL pulse power and phase evolution over multiple passes for the corresponding cavity detunings.

using a 'smooth' Gaussian current profile were also carried out where spontaneous shot-noise emission dominates any CSE during start-up. Figure 8 plots the radiation scaled power and the spectral component of the intracavity FEL output for a detuning case of $2\delta L/\lambda_r = 0.4$. A more noisy initial power output is observed after the first pass through the FEL oscillator, consistent with spontaneous, shot noise emission rather than the CSE of the rectangular beam current of Fig. 5. While the fundamental frequency $\omega/\omega_r = 1$ initially dominates, the power growth of the third harmonic becomes more pronounced with larger pass numbers, particularly in the steady-state.
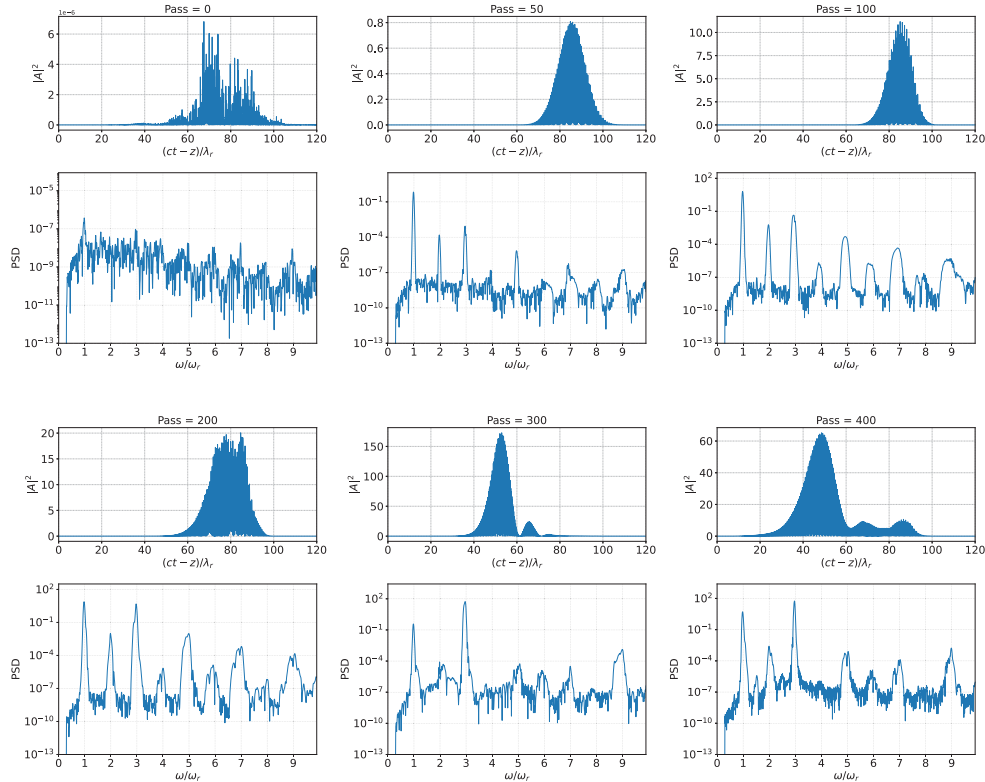

Fig. 8. The temporal, scaled intracavity power profiles, $|A|^2$, at the undulator exit for the central transverse node of the Puffin output field starting from the Gaussian electron beam, and its corresponding power spectral density (PSD), for different pass numbers through the cavity for a cavity detuning of $2\delta L = 0.4\lambda_r$. It can be seen that, while there is initial growth of the fundamental $\omega/\omega_r \approx 1$ from spontaneous shot-noise, the third harmonic $\omega/\omega_r \approx 3$ evolves to dominate at larger pass numbers into the steady state.

The similar effects to the use of a rectangular beam when using the Gaussian electron beam for this behaviour can be seen in Fig. 9, which plots the scaled spectral pulse energy (Fig. 9(a)) for the case of $2\delta L/\lambda_r = 0.4$. It can be seen that the fundamental (solid line) has a greater initial gain, which starts from electron shot noise. The fundamental pulse energy reaches the maximum at pass numbers ~ 190 and begins to decay, while the third harmonic (dashed line) continues to be amplified. The fundamental gain here is smaller to those of the cases of rectangular beam (Figs. 6 and 7) where the FEL starts up from CSE. It can also be seen from the contours plot of the instantaneous pulse power and phase (Fig. 9(b)) that the third harmonic begins to dominate

for pass numbers >200. This third harmonic pulse then continues to be amplified until it reaches a steady-state saturation for pass number >350.
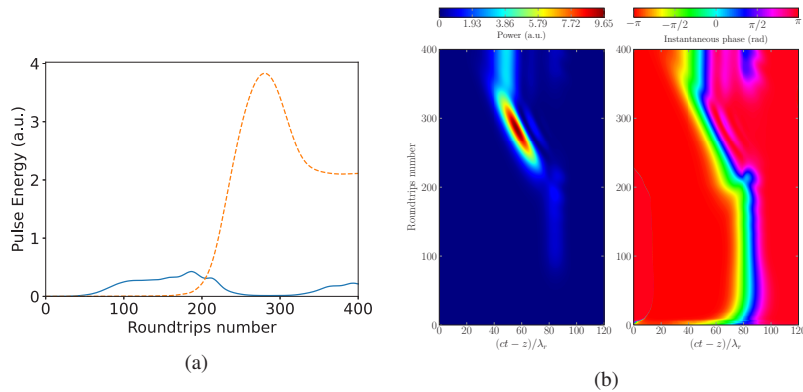

(a)

(b)

Fig. 9. (a) The fundamental (solid blue) and third harmonic (dashed red) spectral pulse energy evolution as the function of cavity roundtrip number for a cavity detuning of $2\delta L = 0.4\lambda_r$. The process starts from Gaussian electron beam current. (b) Contour plot of the FEL pulse power and phase evolution over multiple passes for the corresponding cavity detuning.

As with the rectangular electron beam current profile, simulations using a smooth Gaussian current profile also show that any dominant evolution of the third harmonic into the steady state is also limited to cavity detunings below the fundamental wavelength scale $2\delta L < \lambda_r$, and it can be concluded that the higher pulse energies for the sub-wavelength cavity detuning of Fig. 3(c), are due to harmonic lasing effects. This underscores the role of sub-wavelength cavity detuning as the primary mechanism leading to the harmonic lasing effect, irrespective of either CSE or spontaneous shot-noise being the dominant start up field in the cavity.

4. Conclusion

The use of the coupled Puffin and OPC FEL simulation codes provides a new tool for simulating cavity-based FELs at the sub-wavelength scale, including the effects of coherent spontaneous emission and cavity detuning. The simulations presented here focused, for the first time, on sub-wavelength cavity detuning effects, and demonstrate an unexpected steady-state lasing at the third harmonic.

CSE generation, as modelled here using a rectangular electron beam current shape, has previously been shown generate greater radiation powers than that due to electron beam shot-noise [3]. Such CSE may be able to be utilised to enhance or replace the use of external lasers in seeded cavity FELs, previously studied by [12]. Furthermore, combined with sub-wavelength cavity detuning, the CSE may assist in stabilising, or be used to further enhance the properties of the FEL output. Such effects will typically occur in longer wavelength sources where electron pulse current variations occur more rapidly than in the shorter VUV to X-ray wavelength FELs.

A Gaussian current profile electron bunch, where shot-noise spontaneous emission dominated the CSE, emphasised the role of sub-wavelength cavity detuning in the observed harmonic lasing and validated the phenomenon for different beam current shapes. These findings suggest different new avenues for further exploration into the broader implications and applications of FEL development and technology.

One aspect not studied here is the dynamics of sub-wavelength cavity detuning, e.g. either via noise in the cavity length due to vibrations, or via dynamic adjustment to enhance output. Another, is in the use of crystal optics, used in shorter wavelength FEL designs, which are expected to

differ from the results as presented here for sub-wavelength changes in cavity dimensions. These effects, their feasibility, and other studies, may open up further opportunities and will be the subject of further research.

Disclosures. The authors declare no conflicts of interest.

Data availability. Data underlying the results presented in this paper are not publicly available at this time but may be obtained from the authors upon reasonable request.

References

1. H. Zen, H. Ohgaki, and R. Hajima, "High-extraction-efficiency operation of a midinfrared free electron laser enabled by dynamic cavity desynchronization," Phys. Rev. Accel. Beams **23**(7), 070701 (2020).
2. B. W. J. McNeil, M. W. Poole, and G. R. M. Robb, "Unified model of electron beam shot noise and coherent spontaneous emission in the helical wiggler free electron laser," Phys. Rev. Spec. Top.–Accel. Beams **6**(7), 070701 (2003).
3. B. McNeil, G. Robb, and D. Jaroszynski, "Self-amplification of coherent spontaneous emission in the free electron laser," Opt. Commun. **165**(1-3), 65–70 (1999).
4. L. Campbell and B. McNeil, "Puffin: A three dimensional, unaveraged free electron laser simulation code," Phys. Plasmas **19**(9), 093119 (2012).
5. L. Campbell, B. McNeil, J. Smith, and P. Traczykowski, "An Updated Description of the FEL Simulation Code Puffin," in *Proc. 9th International Particle Accelerator Conference (IPAC'18), Vancouver, BC, Canada, April 29-May 4, 2018*, (JACoW Publishing, 2018), pp. 4579–4582.
6. L. Campbell and B. McNeil, "Puffin: Parallel unaveraged fel integrator," https://github.com/UKFELs/Puffin (2012).
7. J. Karssenberg, P. J. van der Slot, I. Volokhine, J. W. Verschuur, and K.-J. Boller, "Modeling paraxial wave propagation in free-electron laser oscillators," J. Appl. Phys. **100**(9), 093106 (2006).
8. P. J. van der Slot and K.-J. Boller, "Recent updates to the optical propagation code opc," in *Proceedings of FEL*, (2014).
9. J. Karssenberg, P. J. van der Slot, and I. Volokhine, "OPC: Optical propagation code," UTwente, 2006, https://gitlab.utwente.nl/tnw/ap/lpno/public-projects/Physics-OPC.
10. P. Pongchalee and B. McNeil, "Unaveraged simulation of a regenerative amplifier free electron laser," in *39th Free Electron Laser Conference (FEL'19), Hamburg, Germany, 26-30 August 2019*, (JACOW Publishing, 2019), pp. 106–109.
11. S. V. Benson and J. M. Madey, "Demonstration of harmonic lasing in a free-electron laser," Phys. Rev. A **39**(3), 1579–1581 (1989).
12. R. Hajima and R. Nagai, "Generating carrier-envelope-phase stabilized few-cycle pulses from a free-electron laser oscillator," Phys. Rev. Lett. **119**(20), 204802 (2017).
13. J. R. Henderson, B. McNeil, and L. Campbell, "The implementation of 3d undulator fields in the unaveraged fel simulation code puffin," in *36th International Free Electron Laser Conference: FEL 2014*, (2015), p. 416.
14. E. Scharlemann, "Wiggle plane focusing in linear wigglers," J. Appl. Phys. **58**(6), 2154–2161 (1985).
15. B. E. Saleh and M. C. Teich, *Fundamentals of photonics* (john Wiley & sons, 2019).
16. W. B. Colson and A. Renieri, "Pulse propagation in free electron lasers," Le J. De Physique Colloques **44**(C1), C1-11–C1-27 (1983).
17. H. Al-Abawi, F. A. Hoff, G. T. Moore, and M. O. Scully, "Coherent transients in the free-electron laser: Laser lethargy and coherence brightening," Opt. Commun. **30**(2), 235–238 (1979).
18. R. Bakker, D. Jaroszynski, A. van der Meer, D. Oepts, and P. van Amersfoort, "Short-pulse effects in a free-electron laser," IEEE J. Quantum Electron. **30**(7), 1635–1644 (1994).
19. R. Kiessling, W. B. Colson, S. Gewinner, W. Schöllkopf, M. Wolf, and A. Paarmann, "Femtosecond single-shot timing and direct observation of subpulse formation in an infrared free-electron laser," Phys. Rev. Accel. Beams **21**(8), 080702 (2018).
20. N. Piovella, P. Chaix, G. Shvets, and D. A. Jaroszynski, "Analytical theory of short-pulse free-electron laser oscillators," Phys. Rev. E **52**(5), 5470–5486 (1995).